

# Relativistic electrons produced by reconnecting electric fields in a laser-driven bench-top solar flare

J. Y. Zhong<sup>1,3,12</sup>, J. Lin<sup>2</sup>, Y. T. Li<sup>4,11</sup>, X. Wang<sup>5</sup>, Y. Li<sup>2</sup>, K. Zhang<sup>1</sup>, D. W. Yuan<sup>1</sup>, Y. L. Ping<sup>1</sup>, H. G. Wei<sup>1</sup>, J. Q. Wang<sup>6</sup>, L. N. Su<sup>4</sup>, F. Li<sup>4</sup>, B. Han<sup>1</sup>, G. Q. Liao<sup>4</sup>, C. L. Yin<sup>4</sup>, Y. Fang<sup>7</sup>, X. Yuan<sup>7</sup>, C. Wang<sup>8</sup>, J. R. Sun<sup>8</sup>, G. Y. Liang<sup>1</sup>, F. L. Wang<sup>1</sup>, Y. K. Ding<sup>9</sup>, X. T. He<sup>10</sup>, J. Q. Zhu<sup>9</sup>, Z. M. Sheng<sup>7,11,12</sup>, G. Li<sup>10</sup>, G. Zhao<sup>1\*</sup>, J. Zhang<sup>7,12\*</sup>

gzhao@bao.ac.cn, jzhang1@sjtu.edu.cn

Received \_\_\_\_\_; accepted \_\_\_\_\_

---

<sup>1</sup>Key Laboratory of Optical Astronomy, National Astronomical Observatories, Chinese Academy of Sciences, Beijing 100012, China

<sup>2</sup>Yunnan Observatories, Chinese Academy of Sciences, P. O. Box 110, Kunming, Yunnan 650216, China

<sup>3</sup>Department of Astronomy, Beijing Normal University, Beijing 100875, China

<sup>4</sup>Beijing National Laboratory for Condensed Matter Physics, Institute of Physics, Chinese Academy of Sciences, Beijing 100190, China

<sup>5</sup>Department of Physics, Harbin Institute of Technology, Harbin 150001, China

<sup>6</sup>College of Physical Science and Technology, Sichuan University, Chengdu 610065, China

<sup>7</sup>Key Laboratory for Laser Plasmas (MoE) and Department of Physics and Astronomy, Shanghai Jiao Tong University, Shanghai 200240, China

<sup>8</sup>Shanghai Institute of Laser Plasma, Shanghai 201800, China

<sup>9</sup>National Laboratory on High Power Lasers and Physics, Shanghai 201800, China

<sup>10</sup>Department of Space Science and CSPAR, University of Alabama in Huntsville, Huntsville, AL 35899, USA

<sup>11</sup>Department of Physics, SUPA, University of Strathclyde, Glasgow G4 0NG, UK

<sup>12</sup>IFSA Collaborative Innovation Center, Shanghai JiaoTong University, Shanghai 200240, China

## ABSTRACT

Laboratory experiments have been carried out to model the magnetic reconnection process in a solar flare with powerful lasers. Relativistic electrons with energy up to MeV are detected along the magnetic separatrices bounding the reconnection outflow, which exhibit a kappa-like distribution with an effective temperature of  $\sim 10^9$  K. The acceleration of non-thermal electrons is found more efficient in the case with a guide magnetic field (a component of magnetic field along the reconnection-induced electric field) than that in the case without a guide field. Hardening of the spectrum at energies  $\geq 500$  keV is observed in both cases, which remarkably resembles the hardenings of hard X-ray and  $\gamma$ -ray spectra observed in many solar flares. This supports a recent proposal that the hardening in the hard X-ray and  $\gamma$ -ray emissions of solar flares is due to a hardening of the source-electron spectrum. We also performed numerical simulations that help examine behaviors of electrons in the reconnection process with the electromagnetic field configurations occurring in the experiments. Trajectories of non-thermal electrons observed in the experiments were well duplicated in the simulations. Our numerical simulations generally reproduce the electron energy spectrum as well, except the hardening of the electron spectrum. This suggests that other mechanisms such as shock and/or turbulence may play an important role in productions of the observed energetic electron.

*Subject headings:* laboratory astrophysics: magnetic reconnection: solar flares: general  
— particle-acceleration: plasma physics

## 1. Introduction

Energetic particles are ubiquitous in the universe. They show up as cosmic rays, produce synchrotron emission from distant radio galaxies, and appear in solar eruptions, like flares and coronal mass ejections (CMEs), and geomagnetic storms. Those detected in solar eruptions are so-called solar energetic particles (SEPs). It is now largely accepted that there are two SEP events: impulsive and gradual. In gradual SEP events, timing studies and composition of SEPs suggests that these energetic particles are accelerated at a CME-driven shock with a height of several solar radii (Reames 2013). In impulsive events, it is believed that the acceleration of electrons and ions are closely tied to the reconnection process in the flare. Various acceleration mechanisms include reconnection electric field acceleration (Litvinenko 1996), acceleration at magnetic islands (Drake et al. 2006), diffusive shock acceleration at a fast mode shock (Tsuneta & Naito 1998), the 2nd Fermi acceleration by turbulence (Miller et al. 1997). We note that in many large SEP events, flares and CMEs often occur together. So it is possible that multiple acceleration processes can operate at the same time.

Magnetic reconnection is at the core of many dynamic phenomena in the universe (Adriani et al. 2009), for example, geomagnetic substorms, and tokamak disruptions (Priest & Forbes 2000; Biskamp 2000). In these environments, magnetic field may break and reconnect rapidly when twisted and sheared, converting magnetic energy into heat and kinetic energy (Yamada et al. 2007). Because magnetic reconnection occurs in magnetic field reversals or current sheets (CS. Petschek 1964; Sweet 1969; Thorne et al. 2005), a strong electric field is induced in the sheet, which is known as the reconnection-induced electric field (RIE-field).

Part of the kinetic energy is in the energetic particles that are accelerated by the RIE-field inside the CS (Figure 1). Studies of solar flares and the associated SEPs indicated

that up to 10%-50% energy released in the flare was carried by electrons and protons with kinetic energies over 20 keV and 1 MeV, respectively, from the CS (e.g., see Lin & Hudson 1976; Aschwanden 2002; Emslie et al. 2004). In the reconnection process, the magnetic reconnection inflow brings both magnetic field and plasma into the CS, and produces the RIE-field  $\mathbf{E}$ . In the coordinate system shown in Figure 1, protons and electrons are accelerated in opposite direction by  $\mathbf{E}$  along the  $z$ -axis, the  $\mathbf{v} \times \mathbf{B}$  force causes them to oscillate in  $y$ -direction, and a residual magnetic field,  $\delta\mathbf{B}$ , inside CS, deflects them. After being turned  $90^\circ$  by  $\delta\mathbf{B}$ , the accelerated particles eventually leave the CS roughly in the same direction (see Figure 1).

Speiser et al. (1965) investigated particle accelerations by the magnetic reconnection process in the geomagnetic tail for the first time. They found that the final energy of accelerated particles depends on both the electromagnetic (EM) field strength and structures in the CS. Accelerated particles would stay inside the CS forever if no residual magnetic field  $\delta\mathbf{B}$  exists, and the appearance of a component of the magnetic field in the  $z$ -direction (namely the guide field) helps confine the accelerated particles in the CS long enough to gain higher energy. Then, (Martens et al. 1988, 1990) noticed that a CS develops in the CME/flare configuration, and suggested that what happens in the geomagnetic tail may also occur in the CME/flare CS (see also Priest & Forbes 2000).

In the above studies, the acceleration region includes a single Y-type neutral point (Y-point), but the CSs in both the geomagnetic tail and the CME/flare configuration in reality are more likely to include multiple X-points among which a principal one dominates the others (Lin et al. 2005, 2008; Bárta et al. 2011; Shen et al. 2011), and the conversion of magnetic energy into heat and kinetic energy of plasma occurs mainly around the principal X-point (see also Lin et al. 2008). Therefore, the particle accelerations in the CS including a single X-point is usually considered as a local process occurring in a large scale CS (see

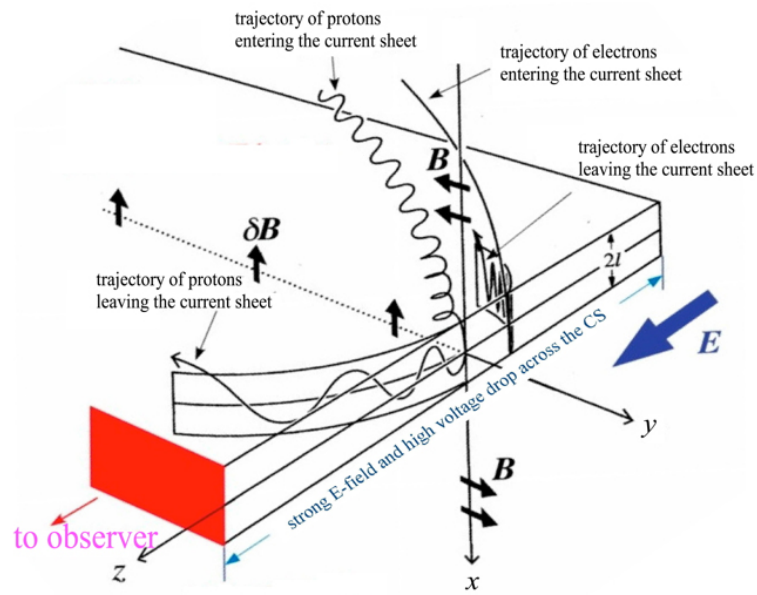


Fig. 1.— Schematic descriptions of a CS configuration, in which  $\mathbf{B}$  is the magnetic field outside the CS,  $\mathbf{E}$  is the induced electric field in the reconnection process, and  $\delta\mathbf{B}$  is the residual magnetic field inside the CS. Trajectories of protons and electrons are described by waving curves. (From Li & Lin 2012.)

Li & Lin 2012; Li et al. 2013; and references therein).

Physical properties of magnetic reconnection and the associated processes occurring inside the reconnection region have also been investigated in laboratory for a while. Recently, the high energy density laboratory astrophysics (Remington et al. 2006) develops quickly. In this field, experiments are performed with intense lasers in laboratory to simulate various astrophysical processes and to probe important features and key properties of these processes, allowing us to look into the physics of these processes. Extensive experiments have been performed and many works have been published within a decade (see also Zhong et al. 2010 and Lin et al. 2015 for a brief review). Although systems in different environments possess very different scales varying over a huge range, scaling laws (Ryutov et al. 2000) of plasma and MHD processes bring them to the same mathematical framework.

**We need also to note here that extra attention must be paid when applying the scaling to the systems of interest if the dissipation takes place in these systems. Ryutov et al. (2000) discussed this issue in detail. They pointed out that a large Lundquist number,  $S_m$ , is a criteria parameter for describing the astrophysical phenomena through MHD equations, and that the ideal MHD condition is a necessity for the validity of the scaling law connecting two systems of different scales in the lab and in the astrophysical environment. When studying the magnetic reconnection process, on the other hand, they further indicated that the same scaling law can also be applied if  $S_m$  is as large as  $10^2 - 10^3$ .**

In the magnetized plasma, the Lundquist number,  $S_m = v_A L / \eta$ , where  $v_A$  is the Alfvén speed and is used as the characteristic speed,  $L$  is the characteristic length, and  $\eta$  is the magnetic diffusivity of the plasma in the system of interest

(In the literature the expression magnetic Reynolds number  $Re_M$  is also used for the  $S_m$ ). Interested readers refer to Priest & Forbes (2000, p. 35) and Priest (2014, p.89) for more discussions. According to Remington et al (2006) as well as Ryutov et al. (2000), the Lundquist number of the system studied in this work is given by  $S_m = 0.8L(\text{cm})\sqrt{(Z+1)/(Z^2A)}[T(\text{eV})]^2$ , we follow the practice of Zhong et al. (2010) and choose  $Z = 13$ ,  $A = 27$ ,  $L = 0.1\text{cm}$ , and  $T = 1000$  eV since the arrangements for both experiments are the same. Here  $Z$  is the charge state of the aluminum (Al) ion in the plasma appearing in our experiments,  $A$  is the relative mass of the Al atom. This gives  $S_m$  around  $4 \times 10^3$ , which apparently exceeds  $10^3$ .

Alternatively, we are also able to estimate the value of  $S_m$  on the basis the rate of magnetic reconnection occurring in this system. As shown by Zhong et al. (2010), the experiment duplicated the main features of the two-ribbon flares, which implied that the reconnection process driven by the powerful laser beams in this kind of experiment is fast. Both analytic studies and numerical experiments have confirmed that the Sweet-Parker-type reconnection is too slow to support the energy conversion required for driving a major eruption like the two-ribbon flare. For the reconnection problem studied here, the Lundquist number for the reconnection region,  $S_R$ , is related to  $v_A$ ,  $\eta$ , and the half-length of the current sheet  $L_{cs}$  in the way of  $S_R = v_A L_{cs} / \eta$ .

Considering the fact that the environment set up for our experiments is similar to that of Nilson et al. (2008) for which Fox et al. (2011) discussed properties of several important parameters. According to discussions of Fox et al. (2011), we are able to deduce the magnetic diffusivity of the system,  $\eta = 1.73 \times 10^{-7} / \mu_0 \text{ m}^2 \text{ s}^{-1}$ . Zhong et al. (2010) found that  $v_A = 4.0 \times 10^5 \text{ m s}^{-1}$ ,

and we could measure the length of the current sheet,  $2L_{cs} = 0.35$  mm, from Figure 3a of Zhong et al. (2010). Estimate  $S_R$  on the basis of the values of these parameters gives  $S_R = 517$ .

Obviously, both results for  $S$  and  $S_R$  are not very different from one another for the case studied in this work, and are also in the range of which the scaling law connecting different systems holds. Therefore, we are allowed to use the MHD scaling law to connect the reconnection processes occurring in the solar eruption and in the laboratory to one another, and parameters for the same physical feature in these two different systems could be well related to one another via equations below:

$$\begin{aligned} r &= ar_1, & \rho &= b\rho_1, & p &= cp_1, \\ t &= a\sqrt{b/ct_1}, & v &= \sqrt{c/bv_1}, & B &= \sqrt{c}B_1, \end{aligned} \tag{1}$$

where  $r$  is the characteristic length,  $\rho$  is the mass density,  $p$  is the gas pressure,  $v$  is the velocity,  $B$  is the magnetic field of the systems, and  $a$ ,  $b$ , and  $c$  are transformation coefficients. The similarity of the MHD in the solar flare and in the “bench-top” flare could be seen with the transformation coefficients  $a = 10^{-11}$ ,  $b = 10^8$ , and  $c = 10^{10}$ , namely the reconnection process occurring in laboratory could be well scaled to that occurring in the solar flare under the condition given in (1) with coefficients of certain values. Interested readers refer to Ryutov et al. (2000) and Zhong et al. (2010) for more details.

The laser-driven magnetic reconnection (LDMR. Li et al. 2007; Nilson et al. 2008; Zhong et al. 2010) is one of the most significant topics of the laboratory astrophysics, booms rapidly and draws extensive attentions lately. Referring to solar X-ray observations, some very similar images were also found in a recent LDMR experiment. Faraday rotation

method (Stamper et al. 1975) was used to measure the magnetic field in laser-produced plasmas, which can be up to a mega-gauss. At that time, the structure of magnetic field was not very clear until the proton radiography technique became available (Nilson 2006; Li et al. 2007 and 2009). With this technique, the magnetic field that is produced in the plasma bubble by the Biermann battery effect (see Biermann 1950; Roxburgh 1966; Widrow 2002) can be measured. Such a magnetic field results from the anisotropic pressure in the plasma when a solid target is intensively irradiated by the long pulse laser and evaporates (nanosecond laser, with intensity of around  $10^{15}$  W cm<sup>-2</sup>).

The magnetic field in the universe is produced by the Biermann battery effect such that the difference in mobility between electrons and ions in an ionized plasma leads to charge separation and the breakdown of the MHD approximation. In a system filled with plasma, non-uniformities in both temperature and density occurs frequently, and the gradient of the gas pressure due to the non-uniformity drives the plasma to move in the direction against the gradient, and electrons move faster than protons and the other heavy ions, resulting in an electromotive force and the associated magnetic flux. In the early universe, the magnetic field produced this way is thought to range from  $10^{-21}$  to  $10^{-19}$  G, which is usually known as the “seed field”, and is too weak to be detected. So the dynamo process is needed to amplify this seed field to a much higher strength, say between  $10^{-7}$  and  $10^{-5}$  G, which can be observed/detected (e.g., see also Widrow 2002 for more details).

In the laboratory environment, on the other hand, the Biermann effect has also been observed in laser-generated plasmas (Stamper and Ripin 1975; also see Loeb & Eliezer 1986). A plasma bubble of strong temperature and density gradients can be created as the intense laser beam irradiates a solid target, and the two gradients are nearly perpendicular, leading to a source term for the magnetic field typically megaGauss in strength. In this case, the “seed” field is already strong enough to allow follow-up experiments to be performed,

so the dynamo process for amplifying the magnetic field is not needed. Because the plasma in the bubble is almost fully ionized, freezing of the magnetic field to the plasma causes the field to expand together with the plasma at high speed.

Yates (1982) realized the occurrence of magnetic reconnection when an unexpected X-ray emission was observed between two laser spots in a multi-beams experiment. As the two bubbles expanded laterally and encountered each other with oppositely directed magnetic fields, reconnection took place and the field lines were topologically rearranged in the diffusion region. Later, with the proton radiography technique, Nilson (2006) and Li (2007) diagnosed the LDMR, and some striking features were found, such as the collimated jets and magnetic null point in the diffusion region.

With long pulse lasers, Zhong et al (2010) constructed LDMR to model the loop-top X-ray source and outflows, which are often observed in solar flares. In their experiments, two Al foil targets were placed on the same plane, and a copper (Cu) target was placed right below the Al targets with its plane perpendicular to the Al plane (see Figure 1 of Zhong et al. 2010). Two plasma blobs were created as the Al targets were irradiated by two intense laser beams. Magnetic fields of opposite polarity associated with the plasma blobs moved toward each other as the blobs expanded, and magnetic reconnection took place between them. Two outflows were observed in the experiments. Downward outflow directly collided the Cu target and produced a very hot X-ray spot, which was used to model the loop-top source of the X-ray emission observed in the two-ribbon flare (see Figure 2 of Zhong et al. 2010). The flow velocity was directly measured to be  $400 \text{ km s}^{-1}$ , which agrees well with the typical Alfvén speed in the lab environment.

Usually, the reconnection region in the laboratory environment, including the tokamak instrument, contains a single X-point. But the characteristic feature of the multiple X-point reconnection, namely plasma blobs included in the CS, was also reported to appear in the

lab experiments (Dong et al. 2012). Plasma blobs flowing in a CS developed by a major eruption were reported by Ko et al. (2003) for the first time, and were observed in many eruptive events afterwards; the numerical experiments by Forbes & Priest (1983) displayed plasma blobs in the reconnecting CS for the first time, then were confirmed by all the subsequent numerical experiments on the related topic (e.g., see a recent review by Lin et al. 2015 for more details).

Li & Lin (2012) and Li et al. (2013) showed that complex structures inside CS play an important role in governing both trajectories and spectra of energetic particles accelerated in the CS. But it is very hard, if not impossible, to observe this process directly and to perform in situ measurements for the energetic particles near the reconnection region in space, so the necessity to conduct the laboratory experiments is apparent. The importance of performing such experiments is three-fold.

First of all, it provides us a unique opportunity to investigate the particle acceleration by reconnection directly because the fundamental physics of this process throughout the universe is the same. So, properties of possible mechanisms for cosmic ray and even  $\gamma$ -ray burst (Yuan & Zhang 2012; Meng et al. 2014), which can hardly be observed directly, might also be inferred from studying the laboratory energetic particles (LEPs) that are accelerated by magnetic reconnection.

Second, the experiments conducted here would demonstrate solid evidence that the RIE-field does accelerate electrons impulsively to high energy, which is suggestive of the important role of the reconnection process in producing energetic particles in the magnetically explosive events throughout the universe. And third, SEPs bring a large amount of energy from the Sun. The energy of individual particles ranges from 10 keV to 1 GeV, which can severely damage satellites and endanger astronauts in space. Therefore, studying the LEPs, looking for their analogy to SEPs, and further understanding the

physics behind SEPs are of great scientific and socio-economic significance.

Following practices of Zhong et al. (2010) and the follow-ups, we designed and performed experiments that allow us to directly detect and study the energetic particles accelerated in the LDMR process. By carefully designing the target orientation and the laser incident angle, two cases are investigated: One undergoes without guide field, and another one with a guide field. In addition to performing the experiment itself and analyzing the consequent data, we shall also theoretically study trajectories and energy spectra of the energetic particles produced in the CS. We do not perform particle-in-cell (PIC) simulations in this work because PIC is very computer-time-consuming, otherwise a small proton-to-electron mass ratio, say between 100 and 200 (Drake et al. 2006), needs to be used. Perez et al. (2013) performed a PIC simulation on the related topic using the real value of the Al ion-to-electron mass ratio, and found that it took a few times  $10^5$  cpu hours to evolve the system over a period of a few ps. To save computer resources and to explore electron accelerations in the reconnection region with the correct proton-to-electron mass ratio, we use test particle approach for our theoretical investigations. The collisionless environment where the experiment occurs (detailed arguments will be given later) also allows us to use this technique to study particle accelerations without considering particle interactions.

In next section, we are introducing the setup of the experiments performed in this work; results of these experiments and the corresponding theoretical calculations will be displayed in Section 3; these results and the physics behind are discussed in Section 4; and finally, we summarize this work in Section 5.

## 2. Setup and Performance of Experiments

We perform experiments using the Shenguang II (SGII) laser facility, which can deliver a total energy of 2.0 kJ in a nano-second (ns) square pulse. Eight SGII laser beams, at wavelength of  $\lambda_L = 0.351 \mu\text{m}$ , are divided into four bunches with each bunch consisting of two laser beams. Figure 2a displays the arrangement of instruments used for the laser-driven reconnection experiments. Two synchronized laser bunches separated by  $600 \mu\text{m}$  are focused on two aluminum (Al) foils with area of  $850 \mu\text{m} \times 500 \mu\text{m}$  and thickness of  $50 \mu\text{m}$ . Each bunch is focused to a focal spot with a diameter of  $50\text{-}100 \mu\text{m}$  at the full width at half maximum (FWHM), generating an incident laser intensity of  $\sim 5 \times 10^{15} \text{ W cm}^2$ . The two Al foils are either located in the same plane, so magnetic reconnection and subsequent processes occur roughly in a 2-D configuration (case 1); or rotated oppositely away from the plane in case 1, so magnetic reconnection and the consequent phenomena of interests would occur in a 2.5-D configuration (case 2), which is the case that a guide field, namely a component of magnetic field in the direction along the RIE-field, is added to a 2-D configuration.

A copper (Cu) target of  $1,600 \mu\text{m} \times 250 \mu\text{m}$  in area and of  $150 \mu\text{m}$  in thickness is placed at  $250 \mu\text{m}$  right below the region between the two Al foils. This Cu target plays a role of the solar chromosphere in experiments, and a “bench-top” solar flare would be created as the downward reconnection outflow and energetic particles accelerated by reconnection bomb it. An X-ray pinhole camera in the upper and forward direction (illustrated by the blue cone) is set for monitoring the reconnection process as well as the impact of the reconnection on the Cu target. The image is taken with a  $10 \mu\text{m}$  pinhole filtered with a beryllium layer of  $50 \mu\text{m}$  allowing all X-ray emission of energy above 1 keV to get through. Most of the signal from a high-energy continuum is time-integrated over 5 ns and recorded on an X-ray film that is most sensitive to X-rays in the energy range from 1 to 10 keV.

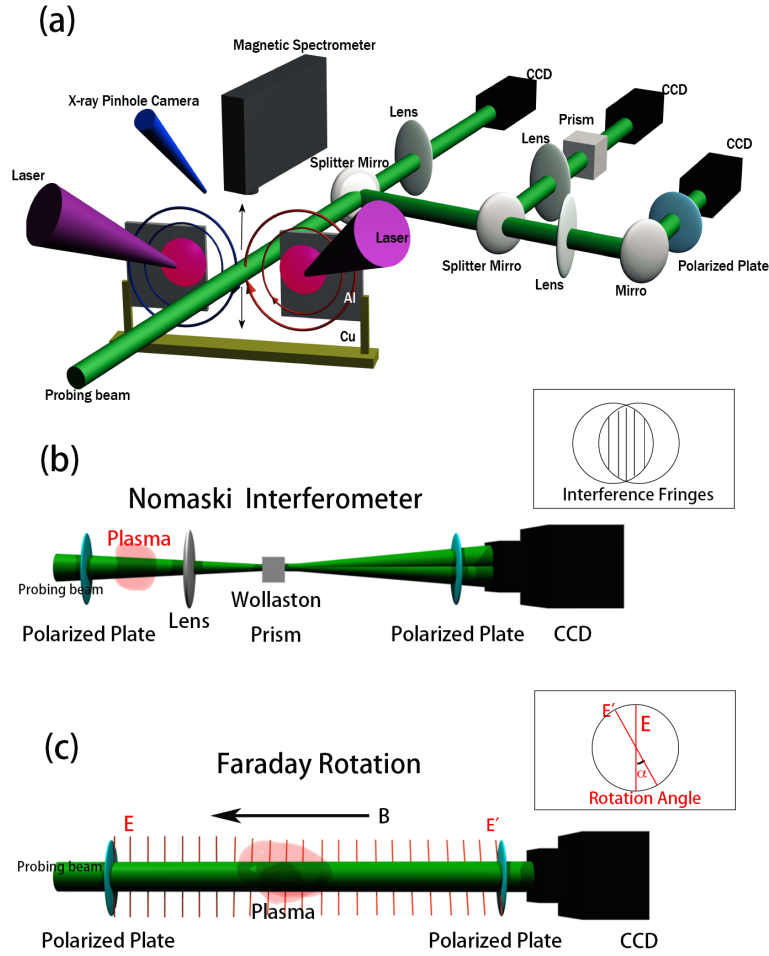


Fig. 2.— (a) Schematic description of the experimental setup for the laser-driven magnetic reconnection and the consequent particle acceleration studied in the present work. In this arrangement, the purple laser beams, the Al and Cu targets, as well as the phenomena occurring on and around them, constitute the focus of this work, and the other instruments shown here are set up for measuring and detecting the output of the experiment. A laser beam represented by those green pipes is shot through the reconnection region for the purpose of diagnoses in the experiment. It is split into three for displaying the plasma structure, measuring the electron density (b), and measuring the Faraday rotation angle (c) and then the magnetic field, respectively, in the reconnection region.

A 1000-Gauss electron magnetic spectrometer (MS, the black box in Figure 2a) is located about 15 cm above the midpoint of the line connecting the centers of the two Al foils, to detect the energetic electrons from the reconnection region, which covers the energy range extending to 2 MeV. The instrument distinguishes the charged particles according to their velocities. In the MS, the incident charged particles are deflected by the magnetic field. Slower particles are deflected more, and faster particles are deflected less, which eventually yields a distribution of the incident particles in space depending their speeds on a given plane in the way particles propagate. In the instrument, an imaging plate, which is a photostimulable phosphor screen deposited on flexible plastic substrates, is placed on such a plane to collect those deflected particles, which results in the read-out of the MS. Calibrating the read-out to the particle energy on the basis of the known responding curves of the instrument, we are able to count the numbers of electrons of different energies.

To describe the setup of instruments, the EM-field occurring in the experiments, and both experimental and theoretical results easily and clearly, we fit the arrangement of instruments in Figure 2 to the Cartesian coordinate system in Figure 1. This is done by performing operations as below:

Rotating the configuration shown in Figure 1 around the  $z$ -axis anti-clockwise by  $90^\circ$  and setting the origin of the coordinate system to the midpoint of the line connecting the two Al-foil centers as displayed in Figure 2a, we have the magnetic fields,  $\mathbf{B}$ , shown in Figure 1 near the reconnection region align to those displayed in Figure 2a. In this system, the  $x$ -axis is along the line connecting the two Al-foil centers pointing rightward in Figure 2a, the  $y$ -axis points upward, and  $z$ -axis points outward from the paper.

In such a coordinate system, we realize that the direction “to observer” in Figure 1 is toward the X-ray pinhole camera and away from the shadowgraphy in Figure 2a, and the MS was arranged such that the surface of its detector faces the origin of the coordinate system

with the center of the detector surface located at the  $y$ -axis. Consulting trajectories of energetic particles (electrons and protons) leaving the acceleration region shown in Figure 1, we know that the MS is in the way of escaping accelerated electrons. In the experiments like we performed here, the charged particle that could be effectively accelerated is mainly electrons because the reconnection process is too short to accelerate protons and heavy ions due to their large inertia.

Behaviors of the plasma in the experiment are recorded by an optical diagnostic device. This device includes three channels of a 30 ps green ( $\lambda_L = 0.532 \mu\text{m}$ ) laser beam (namely the so-called probe beam, represented by the green pipes in Figure 2a), it is employed to help collect the information about the evolution in both the plasma and the magnetic field during the experiment. It is used to freeze the plasma expansion and provide a snapshot of spatial information. Through changing delay between the probe and target beams, the expansion dynamics of experimental plasma can be measured for all channels. As the experiment starts, the probe beam that is polarized (see Figure 2a) is turned on simultaneously, it first goes through the reconnection region, and then is split into three: one is sent to the channel for the shadowgraphy, another one is for the Nomarski interferometer, and the third one is for measuring the Faraday's rotation (refer to Figure 1 of Zhong et al. 2010 as well).

The shadowgraphy is sensitive to the secondary spatial derivative of the refractive index of the plasma, which varies with the plasma density according to the Appleton-Hartree equation (e.g., see also detailed discussions of Budden 1961; and Helliwell 2006, pp. 23 – 24). So it is good at displaying the contours of the plasma density in space. As the probe beam goes through the reconnection region, spatial variations in the plasma refractive index modulate the manifestation of the probe beam, and recording the modulated manifestation helps indirectly represent inhomogeneity or structures of the plasma in space.

The Nomarski interferometer is used to measure the electron density in the reconnection

region by detecting the distortion of the wavefront of the probe beam after going through that region. The distortion is also caused by the non-uniform refractive index of the plasma, which is a function of the electron density. As shown in Figure 2b, the distorted probe beam from the reconnection region is further split by a Wollaston prism into two separate linearly polarized beams. The linear polarizer is oriented at the original polarization angle of the incident probe beam so that the two beams polarize in the same plane to guarantee the interference between them to occur successfully. The two slit probe beams have the same amplitude and the orientations of polarization normal to one another. After passing through a linear polarizer, the two beams interfere, and produce interfering fringes on the imaging plane of CCD. Analyzing these fringes provides us the information of the phase shift of the probe beam after going through the reconnection region, and the electron density in that region is further deduced according to the phase shift.

In addition, the third channel is just set up to measure the Faraday rotation, and then the magnetic field (Figure 2c). The refractive index of the magnetized plasma depends on the magnetic field as well, which causes the plane where the probe wave polarizes to rotate when the wave passes through the magnetic field. This is known as the Faraday’s rotation, and is used to measure the magnetic field in the region of interest. In our experiments, the polarization state of the incident probe beam (or wave) is known and fixed, and that of the probe wave detected at another side of the reconnection region should inevitably change because of the Faraday rotation. At this side, the probe wave including the information of the reconnection region goes through a polarized plate first, and then detected by a CCD (refer to Figure 2c for details). The initial orientation of this plate’s polarization is aligned to that of the incident wave polarization, and the intensity of the probe wave behind the plate detected at this time is not necessarily at its maximum. We then continue to rotate the plate until the intensity at maximum is detected, and the Faraday rotation angle is therefore the difference between the initial orientation of the plate and that when the

maximum intensity appears. This angle is linearly related to the strength of the magnetic field and the length of the path the probe wave propagates (e.g., see also Hutchinson 1987; Li 2000; and references therein for more details). When the instruments used in the experiment are readily arranged, the length of the path of the probe wave is thus fixed, then with the rotation angle being measured, we are able to deduce the strength of the magnetic field.

### 3. Results of Experiments and Theoretical Calculations

With the set-up described in previous section, we are able to perform the experiments of interests. The typical values of plasma parameters for the environment of experiments, such as density and temperature, are the same as those measured with interferometer and X-ray spectroscopy listed in the Table 1 of (Zhong et al. 2010). Hydrodynamic collision effect can also be significant during the merging of the bubbles due to the thermal pressure. Particularly if the thermal pressure is much higher than the magnetic pressure ( $\beta \gg 1$ ), the merging process should be dominated by hydrodynamic collision instead of reconnection, which is the case that occurred in the Omega-laser-scale merging process of a high- $\beta$  experiment with  $\beta \sim 10$ , and the ratio of the separation to the diameter of about unity (Li et al. 2007). Nevertheless, in the present experiments, for the onset of a driven magnetic reconnection, the laser spot separation is nearly 6-7 times the laser focus diameter with a plasma beta of  $\beta = 4.03 \times 10^{-11} n T B^{-2} \sim 1$  (for  $n = 10^{19} \text{ cm}^{-3}$ ,  $T = 1 \text{ keV}$ ,  $B = 10^6 \text{ G}$ ), which is similar to that occurring the Vulcan experiment (Nilson et al. 2008) .

By carefully designing target orientations and the laser incident angles, two cases are investigated: one without guide field (Case 1), and one with a guide field (Case 2). In the coordinate system we have set up (see detailed descriptions given in previous section), our experiments in Case 1 are realized as both the Al foils are located in the  $xy$ -plane, and

those in Case 2 are realized by rotating each Al foil  $15^\circ$  in opposite directions around the  $x$ -axis. As described earlier, the reconnection process studied in this work takes place as a result of the interaction of two fast expanding magnetized plasma bubbles on the Al-foils. So, on one hand, if the two Al-foils are arranged in the same plane as we do for Case 1, magnetic reconnection roughly occurs in a 2-dimensional fashion; on the other hand, if the two Al-foils are not in the same plane, instead an angle exists between the planes where the two Al-foils are located, as we arranged for Case 2, a guide field along the  $z$ -axis the is hence created in the system, and magnetic reconnection happens in a 2.5-dimensional fashion (see also discussions by Li & Lin 2012; Zhakova et al. 2011; Li et al. 2013 ).

In case 1, the EM field possesses the form:

$$\begin{aligned} B_x &= 2y, & B_y &= 4x(1 - x^2), & B_z &= 0, \\ E_z &= \exp\{-[(4x - 4x^3)^2 + (2y)^2]^{1/2}\}, \end{aligned} \quad (2)$$

with the length scale of  $300 \mu\text{m}$  (the half distance between two Al foil centers), the magnetic field in units of  $B_0 = 1.2 \times 10^6 \text{ G}$ , and the electric field in units of  $E_0 = 3 \times 10^8 \text{ V/m}$  (Nilson et al. 2008). In case two, on the other hand, magnetic field generated on each Al foil contributes a  $\cos 30^\circ$  component for reconnection on the  $xy$ -plane, and contributes a  $\sin 30^\circ$  component for the guide field, which is a component of the magnetic field along the RIE-field (Litvinenko 1996; Zharkova et al. 2011). So we have a guide field of  $2B_0B_y \sin 30^\circ$  along the  $z$ -axis in the reconnection region, and two reconnecting fields of  $B_0 \cos 30^\circ$  of opposite polarity. The E-field in the  $z$ -axis does not change its basic pattern as given above, but its strength decreases to  $E_0 \cos 30^\circ$  accordingly. Therefore, the EM field becomes

$$\begin{aligned} B_x &= 2y \cos 30^\circ, & B_y &= 4x(1 - x^2) \cos 30^\circ, & B_z &= 8x(1 - x^2) \sin 30^\circ, \\ E_z &= \exp\{-[(4x - 4x^3)^2 + (2y)^2]^{1/2}\} \cos 30^\circ, \end{aligned} \quad (3)$$

in the second case with units remaining same as those in (2).

Motions of charged particles in the EM-field described by equation (2) or (3) are governed by

$$\frac{d\mathbf{r}}{dt} = \frac{\mathbf{p}}{m_0\gamma}, \quad \frac{d\mathbf{p}}{dt} = e(\mathbf{E} + \frac{1}{c}\mathbf{v} \times \mathbf{B}) - \nu_{eff}^*\mathbf{p}, \quad (4)$$

where  $m_0$  is the rest mass of the charged particle,  $\mathbf{r}$ ,  $\mathbf{p}$ , and  $\mathbf{v} = \mathbf{p}/m_0\gamma$  are position, momentum, and velocity vectors of the particle, respectively,  $\gamma = 1/\sqrt{1 - v^2/c^2}$  is the Lorentz factor with  $c$  the light speed in vacuum, and  $\nu_{eff}^*$  is the effective collision rate (frequency):

$$\begin{aligned} \nu_{eff}^* &= \nu_{eff} \frac{v}{v_{Te}}, & \text{for } v < v_{Te}, \\ \nu_{eff}^* &= \nu_{eff} \left(\frac{v_{Te}}{v}\right)^3, & \text{for } v > v_{Te}, \end{aligned} \quad (5)$$

where  $v_{Te}$  is the thermal velocity of electrons,  $v_{Te} = \sqrt{2kT_e/m_e}$  with  $m_e$  and  $k$  being the electron mass and Boltzmann constant, respectively, and  $\nu_{eff}$  is the sum of the electron collision rate,  $\nu_e$ , and the ion collision rate,  $\nu_i$ , namely  $\nu_{eff} = \nu_e + \nu_i$ :

$$\begin{aligned} \nu_e &= 2.91 \times 10^{-6} n_e \ln \Lambda T_e^{-3/2}, \\ \nu_i &= 4.80 \times 10^{-8} Z^4 \mu_m^{-1/2} n_i \ln \Lambda T_i^{-3/2}, \end{aligned} \quad (6)$$

where  $\ln \Lambda$  is the Coulomb logarithm, which is about 13 for the case we are studying here,  $Z = 13$  is the charge state of the ion occurring in our experiments (see also Zhong et al. 2010),  $\mu$  is the ion mass in units of the proton mass,  $\mu_m = m_i/m_p = 27$ ,  $n_e$  and  $n_i$  are electron and ion density, respectively, with  $n_e = 10^{19} \sim 10^{20} \text{ cm}^{-3}$  and  $n_i = 10^{18} \text{ cm}^{-3}$ ,  $T_e$  and  $T_i$  are electron and ion temperatures, respectively, with  $T_e = T_i = 1.1605 \times 10^8 \text{ K}$  in the cases of interest (see also Zhong et al. 2010). In such an environment, we have  $v_{Te} = 5.9311 \times 10^9 \text{ cm s}^{-1}$ ,  $\nu_i = 3.4299 \times 10^5 \text{ s}^{-1}$ , and  $\nu_e = 3.7830 \times 10^5 \sim 10^6 \text{ s}^{-1}$ , respectively, which implies the impacts of collisions among electrons and of that between electrons and ions on the acceleration process are roughly at a same level. For simplicity, we take  $\nu_e = 10^6 \text{ s}^{-1}$  in our calculations.

The collision term in equation (5) is due to Coulomb interactions between electrons and ions only, and does not include the effect of the turbulent magnetic field in the reconnection region. The effect of the turbulent magnetic field on the motion of charged particles, can be treated as “effective” collision centers. For the time being, on the other hand, the turbulent behavior of the magnetized plasma in the reconnection region is unknown, we therefore do not consider in our theoretical calculations regarding particle accelerations, but stay with the simple motion pattern of electrons governed by equations in (4). We understand that any discrepancy between theoretical results obtained this way and experimental ones may be due to the presence of the MHD turbulence and/or the shock occurring in the experiment.

As an example, we plot the local magnetic field configuration around the CS (continuous and colorful curves) for Case 2 in Figure 3, and the configuration is governed by equations in (3). Parameters for this plot were given as before,  $B_0 = 1.2 \times 10^6$  G,  $E_0 = 3.0 \times 10^8$  V m<sup>-1</sup>, and  $\nu_e = 10^6$  s<sup>-1</sup>, and the electrons initially distribute in the acceleration region randomly (or uniformly). In this EM field, electrons are accelerated **by magnetic reconnection**, and move in the way governed by equations in (4). The theoretical distributions of these electrons in this region as represented by those discrete dots around 4.3 pico-seconds (ps) after reconnection commenced are also plot in Figure 3. As expected, most electrons in this case tend to get together around a surface of which its projection to a plane is known as the separatrix (see below for the discussions about Figure 4). In the field of solar physics, this surface is generally known as the quasi-separatrix layer (QSL, e.g., see Mandrini et al. 2015; Janvier et al. 2015; and references therein). Since the energetic electrons play an important role in heating lower solar atmosphere during the solar flare, the behavior of energetic electrons shown in Figure 3 helps explain why heating and flare ribbons are always observed to occur around the region where QSLs exist (see Janvier et al. 2015 and references therein).

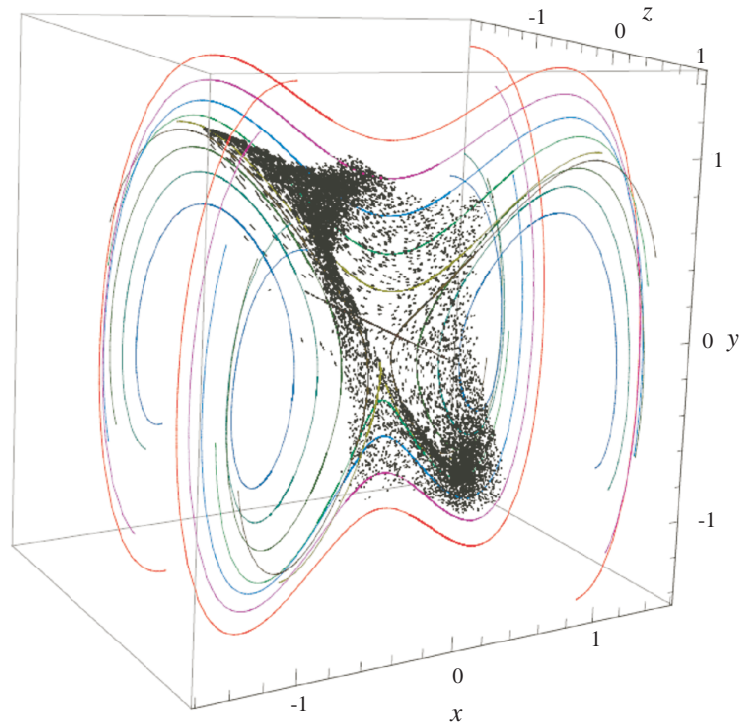


Fig. 3.— The magnetic configuration (continuous curves) around the reconnection region in Case 2 described by equations in (3), and the resultant electron distribution in space around 4.3 ps after the acceleration is initiated. Motions of electrons in this region are governed by equations in (4)

The output of experiments performed in the setup of instruments displayed in Figure 2 with the EM field described by equations (2) and (3) is three-fold (see Figures 4 and 7). First, we obtain shadow images by the shadowgraphy, which shows trajectories of energetic electrons that have left the reconnection region; then, the reconnection outflow and the consequence of its interaction with the Cu target are observed by a pinhole X-ray camera; and third, the energetic electrons accelerated by reconnection are collected by MS and their energy spectra are then deduced. Among these issues, the energy and trajectories of the electron are governed by equations in (4), and the behavior of the reconnection outflow is governed by MHD equations that need to be solved in different numerical approach. Since Zhong et al. (2010) already gave the relevant numerical results for a similar experiment, we do not duplicate them here but just re-show some existing results to help demonstrate the effect of the guide field on the reconnection outflow. In the work below, we first discuss behaviors of the trajectory of energetic electrons and the reconnection outflows, and then look into the energy spectra of these particles collected in our experiments.

### 3.1. Behaviors of Energetic Electrons and Reconnection Outflows

The laser-produced magnetic systems in the experiments are represented by the two solid ellipses in the left panels of Figures 4a1 and 4a2 for Cases 1 and 2, respectively; and the grey contours in the right panels describe the trajectories of the energetic electrons accelerated by the reconnection processes occurring in the above systems consequently. They are shadow images obtained by the shadowgraphy as a probe beam passes through the region around the reconnecting magnetic structures shown in the left panels 2.5 ns after the main laser pulse peaks.

We see two major distinct beams forming a V-shape ejecting from a dark area below in Figure 4a1. Because the plasma density is high in that dark area, the probe beam is

completely blocked, so the plasma situations cannot be known for this area. Instead we are using a pinhole X-ray camera to watch it. Here, we apply dashed contours in the dark region to specifying the location and topology of the magnetic fields where reconnection takes place. Trajectories of energetic particles leaving the acceleration region imply that the electron is the only species that are accelerated in the experiments performed here. More discussions on this issue will be given later.

As we mentioned earlier, what happened in the magnetic configuration shown in Figure 4a1 is a pure 2-D reconnection process without guide field. To check whether the V-shape grey contours were of real energetic electrons accelerated by reconnection, we displayed in Figure 4b1 a theoretical result for a group of electrons moving in the EM field given in equation (2). As expected, most of electrons in such an EM field eventually leave the acceleration region along the four separatrices of the magnetic system, constituting a region of X-shape where particles accumulate. When half of this region is not visible, we see a V-shape region. This indicates that the grey contours displayed in Figure 4a1 were indeed the consequence of 2-D magnetic reconnection.

Unlike Figure 4a1, Figure 4a2 displays different scenario such that distinct major beams ejected almost in one direction. Consulting the setup for the experiment, we know that magnetic reconnection in this case takes place in a configuration including a guide field, which is a component of the magnetic field parallel or anti-parallel to the RIE field. As pointed out by Li & Lin (2012) and Li et al. (2013), the existence of the guide field in a reconnecting magnetic structure helps accelerated particles obtain more energy and changes the trajectory of the energetic particles such that electrons leave the acceleration region almost along one separatrix. Carefully studying the motions of electrons in the EM field described by equations in (3), we end up with trajectories of these electrons as shown in Figure 4b2, of which the continuous and zigged curves, respectively, are projections of

field lines and trajectories of some of particles displayed in Figure 3 onto the  $xy$ -plane. We notice that Figure 4b2 manifests the main features shown in Figure 4a2.

Furthermore, looking into details in both Figure 4a1 and Figure 4a2, we notice that besides major beams, many minor ones randomly distributing around the major beams can also be recognized. This is very likely to imply the inhomogeneity of the reconnection process, which is similar to those observed in a CS usually developed in a real CME/flare event (e.g., see also a recent review by Lin et al. 2015). Scattering of energetic electrons by the inhomogeneous structures inside the CS may cause some electrons to leave the CS randomly (see also Li & Lin 2012 and Li et al. 2013 for more discussions), which might account for those randomly distributed minor beams in both cases.

To investigate the impact of the initial location of electrons on the distribution of accelerated electrons, we also study the acceleration of electrons that initially distribute on the  $xy$ -plane in the Gaussian fashion. The parameters for the EM-field remain unchanged. Duplicating our previous calculations for Figures 3, 4b1, and 4b2, we obtain the distribution of energetic electrons 4.3 ps after the acceleration starts (Figure 5a), the trajectories of some accelerated electrons in the configuration without guide field (Figure 5b), and energetic electron trajectories in the configuration with guide field (Figure 5c). Comparing Figures 5a, 5b, and 5c with Figures 3, 4b1, and 4b2, respectively, we can see that the basic features of both particle distributions and trajectories are the same in the two cases. This indicates that the initial distribution of electrons does not apparently affect either the distribution of accelerated electrons in the reconnection region or the trajectories these electrons leave the acceleration region.

In addition to the energetic electrons, the associated reconnection outflows are also observed by the pinhole X-ray imaging technique, which provides images obtained forward of the Al foil targets (see Figures 6a and 6b). These images display the patterns of

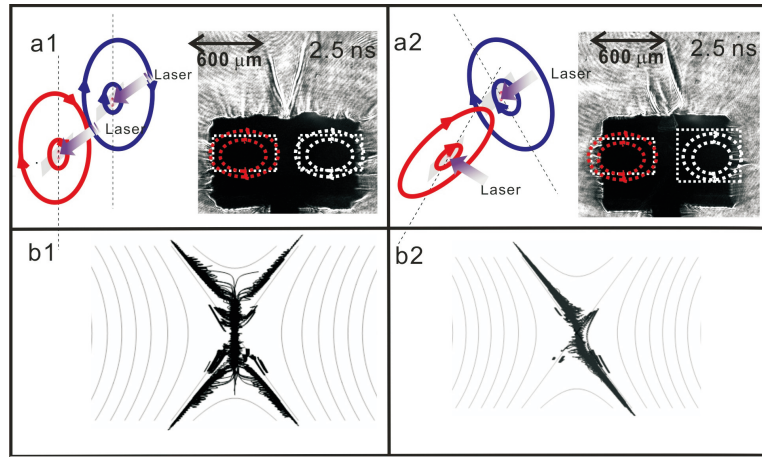


Fig. 4.— Comparisons of experiment and numerical simulation results. (a1)-(a2), Two laser bunches produce two plasma bubbles (in left panels) entangled by magnetic fields without (a1) and with (a2) a guide field, respectively. (b1)-(b2), Results from theoretical calculations for particle accelerations that almost duplicate the results given in (a1) and (a2), respectively.

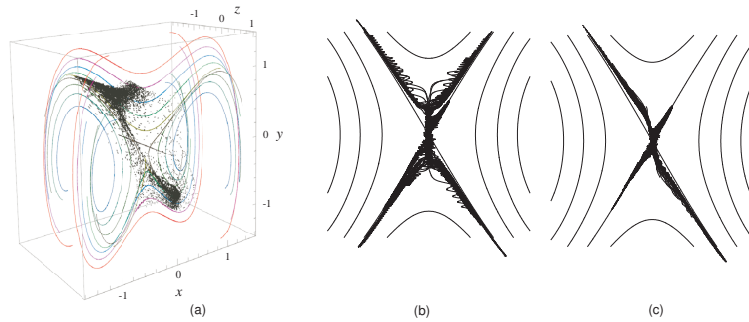


Fig. 5.— For the Gaussian distribution of electron initial positions on the  $xy$ -plane, and about 4.3 ps after the acceleration commences, distributions of energetic particles around the acceleration region in Case 2 (a), trajectories of some energetic particles on  $xy$ -plane in Case 1 (b), and trajectories of some energetic particles in Case 2 (c).

the reconnection outflows as well as consequences of interactions of the outflow and the energetic electrons with the Cu target below, which manifests the scenario of a bench-top solar flare, a laboratory counterpart of the flare in the solar atmosphere produced by the similar process. Panels in Figures 6a and 6b display the interior of the reconnection region. Contours with arrows are for the magnetic structures like those in Figure 4a with colors for fields of different orientation. The red arrow specifies the reconnection outflow, and the black arrow indicates the X-ray emission area produced by the interaction of the reconnection outflow with the Cu target. Like energetic particles, the orientation of the reconnection outflow is apparently affected by the guide field as well.

We further notice that the inhomogeneity in the reconnection region looks less apparent in Figure 6a than that in Figure 6b, which is implicitly suggestive of the role of the guide field in formation of small structures in the reconnection region. These structures are quite likely to result from the turbulence occurring in the reconnection region. Ni et al. (2015) indicated that the turbulent features in the current sheet appeared more easily in the environment with guide field than in that without guide field. But their results showed no effect of the guide field on the direction of the reconnection outflow.

However, the effect of the guide field on the reconnection outflow seems to vary from case to case. Tharp et al. (2012) performed a systematic investigation into guide field effects on collisionless reconnection in a laboratory plasma with the the Magnetic Reconnection Experiment (MRX) of the Princeton University. Their results indicated the effect of the guide field on both the rate of magnetic reconnection and the orientation of the reconnection outflow. Pritchett & Coroniti (2004) explored the physics of 3-D guide-field reconnection using a PIC model in which the particle flows and magnetic flux are free to escape from the system along the magnetic field lines (see also Pritchett 2001). They found that the guide field manifested apparent impact on the motions of ions and electrons, but

almost no impact on the reconnection outflow. Frank et al. (2006) performed another set of experiments for reconnection in laboratory similar to those by Tharp et al. (2012), but with plasmas consisting of various heavy ions: Ar, Kr, and Xe (see also Frank 1999; Bogdanov et al. 2000; and Frank & Bogdanov 2001). The reconnecting magnetic field included a singular X-line and a guide field along the X-line. They found that the CS became tilted and asymmetric, which differed significantly from the scenarios of magnetic reconnection taking place in the plasma with light ions, and the heavier the ions are, the more tilted the CS is. Considering the fact that the magnetic reconnection process studied in the present experiment takes place in the plasma of Al ions, which are much heavier than those of Ar, Kr, and Xe, we conclude that the difference in the reconnection outflow patterns displayed in Figures 6a and 6b results from the combination of the effects of heavy ions and the guide field on the magnetic reconnection process.

### 3.2. Spectra of Energetic Electrons

The data collected by the MS (refer to Figure 2) include the information of the particle energy. Using these data, we are able to deduce the number of electrons per unit energy  $dN/dE$  at a given energy  $E$ , and plotting  $dN/dE$  versus  $E$ , as shown in Figure 7a for Cases 1 (black curve) and 2 (red curve), respectively, gives the differential energy spectrum of the particles. Figure 7a plots one set of data for each case as an example. Both curves include a thermal component at low energy (below 200 keV), and a non-thermal component at high energy (above 200 keV). This is a so-called Kappa-like-distribution (see also discussions of Kasparová & Karlický 2009 and Bian et al. 2014), which is quasi-Maxwellian at low and thermal energy band and decreases as power law at high and non-thermal energy band. The joint between the thermal and non-thermal components on these curves determines an “effective temperature”, which is about  $10^9$  K for the data collected in our experiments.

Existence of the thermal component of energetic particles with a very high effective temperature implies the occurrence of the intense heating in the process of the particle energization.

What is remarkable is that the spectra in both cases show an apparent hardening in the energy range of  $E > 500$  keV, which indicates that the non-thermal part of the energy spectra of particles include two components, a soft one and a harder one, and they join at  $E \approx 500$  keV. Fitting the soft one to a power law function results in an index of around 2.5 for Case 1, and an index of around 2.6 for Case 2; and fitting the harder component gives the indices of 1.5 and 1.6 for Cases 1 and 2, respectively. Occurrence of hardening at the tail of the spectrum indicates that some certain mechanisms work to enhance the particle acceleration in the reconnection region, bringing more particles to the high energy range. We are discussing possible mechanisms in the next section.

Besides their similarity, the difference between these two curves is also apparent. The maximum of the  $dN/dE$  versus curve for Case 2 shifts by 40 keV towards higher energy comparing to that for Case 1. This is suggestive of the increase of the acceleration efficiency as a result of the existence of the guide field. At low energy, the two curves differ when the energy is below 70 keV. The percentage of particles with energy over 70 keV in Case 1 is about **42.0%**, and it increases to **66.0%** for Case 2. Theoretical investigations by Li & Lin (2012) and Li et al. (2013) indicated that the fraction of electrons accelerated from thermal energy in the solar flare region to energies higher than 20 keV is about 0.2 % in the case without guide field, and this fraction could reach up to 5 % as a guide field exists.

With the EM field configuration occurring in the experiments given by equation (2) or (3), together with the associated parameters, we are also able to investigate the energy spectra of energetic electrons for different cases. Initial locations of the electrons may affect the final state of the accelerated electrons, but the way they are brought into the

reconnection region manifests weak impact. Results of Li et al. (2013) indicated that the final state of the accelerated electrons does not depend on the initial locations of these electrons and the way they enter the reconnection region in the case of no guide field, and that the final state does depend on their initial locations, but not the way they enter the reconnection region, in the case with guide field. This suggests that the guide field helps the reconnection process choose the electrons at specific initial locations to accelerate, and leave those out of these locations un-accelerated; however, the role of the guide field is not sensitive to the way the electrons enter the acceleration region. So for simplicity, we start our calculations by assuming that all the electrons accelerated by reconnection initially distribute in the reconnection region randomly for both cases.

Behaviors of  $5 \times 10^6$  electrons in the EM field described by equation (2) or (3) are studied, these electrons move along two separatrices and leave the acceleration region in Case 1 as shown by Figure 4b1, or move and leave the acceleration region along one separatrix in Case 2 as shown in Figures 3 and 4b2. In addition to the trajectory, the final energy of the accelerated electrons is another important issue that we investigate in this work. Considering the location of MS in the setup of the instruments for our experiments (see Figure 2a) and following the practice of Li & Lin (2012), we count the number of electrons that leave the acceleration region along the upper separatrices as shown in Figures 4a and 4b2, and calculate their energies as they reach MS. We then deduce  $dN/dE$  for these electrons according to our calculations, and plot theoretical  $dN/dE$  versus  $E$  curves together with the experimental ones in Figures 7b and 7c for comparison.

When studying the impact of the electron initial distribution on motions and distributions of the the accelerated electron, we have obtained the electron spectrum as well for the case that the initial distribution of electrons in the acceleration region is Gaussian. It turns out that the acceleration of electrons with the Gaussian initial distribution is slightly

more efficient than that with the uniform initial distribution. Figure 8 displays the energy spectra of energetic particles in various cases for comparison. Calculations show that with a Gaussian initial distribution on  $xy$ -plane, about 46.0% and 68.6% thermal electrons could be accelerated to the energy exceeding 70 keV in the EM-fields without and with guide field, respectively. Furthermore, theoretical results are also compared with experimental ones as shown in Figure 9, which indicates the efficiency of acceleration is slightly higher in this case than that with a uniform initial distribution of thermal electrons.

On the other hand, although the calculated spectra in the range from 200 to 500 keV agree fairly well with the experimental ones, they fail to fit the thermal and the hardening components. This suggests that in addition to that the plasma is heated and charged particles are accelerated by the simple RIE-field in the reconnection region, some extra processes/mechanisms may occur inside the same region as well that account for hardening of the energy spectra at the tail, which means that these processes/mechanisms should be able to further diffuse more accelerated particles to higher energies. Obviously, simple and quasi-static EM field does not possess such a capability, turbulence associated with inhomogeneous complex structures in the CS (Lazarian et al. 2012; Drake et al. 2006; Bárta et al. 2011; Shen et al. 2011) as shown in Fig. 6b, and/or perhaps shock structures as suggested by Kong et al. (2013) and Li et al. (2013b), are quite likely to exist in the reconnection region and play an important role in hardening the spectrum.

#### 4. Discussions

Following the practice of Zhong et al. (2010), we performed a set of the LDMR experiments to look into kinetic and dynamic properties of energetic electrons created by LDMR. These electrons were accelerated in a short time interval, and the energy spectrum of these electrons includes the thermal component, and the joint of the thermal

and non-thermal components indicates that the “effective” temperature of the acceleration region was up to  $\sim 10^9$  K. This simply suggests that the intensive heating of plasma and the energetic acceleration of electrons take place simultaneously in the same region. Considering the time scale of acceleration and heating, we point out that these energetic electrons were indeed accelerated by reconnection. Although the fast mode shock in the magnetized plasma can also heat plasma and accelerated charged particles simultaneously, its efficiency heating plasma and accelerating particles is low compared to that of the reconnection process (e.g., see also more details in Miller 1998; Reames 1998; Priest & Forbes 2000; Reames 2013; and references therein). Considering the fact that the time interval of the LDMR process is very short (a few ns) and Al ions are much heavier than electrons, we conclude that the electron is the only species of particles that are accelerated in our experiments.

Theory about the charged particle acceleration by magnetic reconnection in the configuration including a single X-point indicates that energetic electrons leave the acceleration region roughly along four separatrices in the case without guide field (Case 1. cf. Figures 4a1, 4b1, and 5b), our experiments confirmed this result such that trajectories of energetic electrons constitute a V-shape image in the shadowgraphy picture (the image of the upside-down V seen in the theoretical result cannot be seen because of the specific design of the instrument); and the experiment also confirmed the theoretical result for the case with guide field such that the energetic electron leaves the acceleration region along two specific separatrices (Case 2. cf. Figures 4a2, 4b2, and 5c. Again, electrons move along one separatrix cannot be shown in the shadowgraphy picture). Interested readers may also refer to discussions of Zharkova et al. (2011), Li & Lin (2012), and Li et al. (2013) for more details.

It is also worth noticing that the initial state of electrons does not affect the kinetic

behavior of energetic electrons in an apparent fashion. We studied in theory the distribution and trajectories of energetic electrons inside and around the acceleration region with different initial distribution of these electrons, and found that we obtain almost the same result (comparing Figure 3 with Figure 5a, and comparing Figures 4b1 and 4b2 with Figures 5b and 5c, respectively). Regarding the dynamic behavior of energetic electrons, on the the other hand, the initial distribution of electrons manifests some impact on the final energy of these electrons. Our results suggest that the efficiency of the acceleration starting with a Gaussian distribution of electrons is slight higher than that of the acceleration starting with a uniform distribution (cf. curves in different colors in Figures 8a and 8b).

Besides the fact that theoretical results fit part of experimental ones, we can also see that the non-thermal component of the energy spectra obtained from experiments becomes hardening at high energy ( $> 500$  keV), to which our theoretical results do not fit. This reminds us of the hardening of the continuum spectrum at high energies (usually hard X-ray and  $\gamma$ -ray emissions of  $\geq 300$  keV) that has often been observed in many solar flares (Suri et al. 1975; Silva et al. 2000; Share et al. 2006; Kong et al. 2013; Li et al. 2013b; Asai et al. 2013). Among the evidences that we collect so far, the shape of hard X-ray spectrum for the  $\gamma$ -ray flares does not much vary from flare to flare, and the spectra start to harden apparently at energy about 400 keV (e.g., see Yoshimori et al. 1985). Kong et al. (2013) performed a survey of 185 flares on the basis of the data obtained by the Solar Maximum Mission satellite, and identified 23 electron-dominated events whose energy spectra displayed apparent hardening at high energy. They found that the energy spectrum index in low energy ranges from 4.29 to 2.58, and that in high energy ranges from 2.22 to 1.56, comparing with the indices of the energy spectra of around 2.5 in low energy and 1.5 in high energy, respectively, deduced from our experiments for the energetic electrons (see Figure 7a).

Because the hard X-ray and  $\gamma$ -ray emissions observed in the solar eruption is usually believed to result from the bremsstrahlung due to the collision of energetic particles with a background plasma of density sufficiently high that the accelerated electrons are collisionally stopped in the corona (Xu et al. 2008), or due to streaming of these particles through the corona and impacting on the chromosphere (cf. Benka & Holman 1994; Miller et al. 1997; Emslie et al. 2003), it has been speculated that such a hardening reflects an intrinsic hardening in the source-electron spectrum (Suri et al. 1975; Share et al. 2006; Asai et al. 2013). Our experiment, by detecting the energetic electrons directly, confirms this speculation. Explaining a hardening spectrum is not a trivial job, but a recent attempt suggested that a finite-width diffusive shock with whistler-like turbulence may harden the spectrum (Kong et al. 2013; Li et al. 2013b).

In our experiment, however, no knowledge of the turbulence spectrum (TS) and whether the conditions specified by Li et al. (2013b) could be satisfied is available. We shall not further look into the physics of hardening of spectrum in this work, but point out that the reconnection region is actually an assembly of structures of various scales and the associated processes (e.g., see a recent review by Lin et al. 2015), and the turbulent structures that satisfy the conditions set by Li et al. (2013b) should exist. In principle, hardening of the electron spectrum at the high energy end results from interactions of accelerated electrons with these structures, and having understood behaviors of them will allow us to determine TS. Therefore, unresolved questions in this work constitute two tasks for our works in the future: First, design and perform the experiments in laboratory that allow us to explore the reconnection region so that the fine structures in the region and then the functional behaviors of TS could be determined; second, design and perform numerical experiments of magnetic reconnection, similar to those by Bárta et al. (2011), Shen et al. (2011), and Mei et al. (2012), to figure out the property of TS in the reconnection region. With TS known, we are able to study in detail the physics behind the hardenings of the

electron energy spectra and the continuum spectrum of hard X-ray and  $\gamma$ -ray observed in the LDMR experiment and the solar flare.

In addition to the behavior of energetic electrons, we also paid some attention on the reconnection outflow, especially on its response to the existence of guide field. In the case without guide field, our experiments, so as those of Zhong et al. (2010), indicate that the reconnection outflow moves just along the  $y$ -axis. But the direction of the outflow changes and many small structures were observed in the reconnection region as the guide field was imposed (cf. Figures 6a and 6b). Numerical and laboratory experiments indicated that the turbulent structure appears in the reconnection region with guide more easily than in the region without guide field (Ni et al. 2015), and that the heavier the plasma ions are, the more apparent the impact of the guide field on the reconnection outflow are (Frank et al. 2006). Therefore, the occurrence of those small structures in the reconnection region and the change in the direction of the reconnection outflow observed can be ascribed to the impact of the guide field on the reconnection process taking place in a plasma including heavy ions (e.g., Al ions in our experiments).

## 5. Conclusions

A bench-top "solar flare" produced in laboratory with high energy lasers can simulate the loop-top X-ray emission and the outflow/jet due to magnetic reconnection (Zhong et al. 2010), similar to what occurs in a real solar flare. In addition, energetic particles, including electrons and ions, are also consequences of the reconnection process in the flare. Since in situ detection of energetic particles in real flares is difficult, the bench-top "solar flare" is an ideal platform to look into the related particle acceleration processes closely. We have performed a series of experiments for this purpose with both 2-D and 2.5-D magnetic configurations. These are achieved by carefully setting orientations of targets and laser

beams, which allows the reconnection to occur for two cases without or with the guide field. The main results of this work are summarized as follows.

1. Energetic electrons that escape from the magnetic reconnection region were detected. Their trajectories are located at the same place, namely co-located, in space, with the separatrices of the reconnecting magnetic field. Accelerated electrons move along both pairs of separatrices extending from the X-point in the case without the guide field; and they were confined to one pair of separatrix in the case with the guide field. This confirmed the theoretical results (e.g., see Pritchett & Coroniti 2004; Murphy et al. 2008; Zharkova et al. 2011; Li & Lin 2012; Li et al. 2013; and references therein).

2. Only electrons are accelerated in the experiment because the magnetic reconnection takes place in a short time interval and ions are too heavy to respond to the RIE-field in the reconnection region.

3. The energy spectrum of accelerated electrons includes thermal and non-thermal components, and the joint of the two components indicated an effective temperature up to  $10^9$  K. This implies that the energized electrons were originally from the hot plasma that was intensively heated by reconnection.

4. The initial position of electrons do not apparently affect the kinetic behavior of accelerated electrons eventually, but it does affect these electrons' dynamic features such that the efficiency of acceleration is higher in the case that these accelerated electrons initially distribute on the  $xy$ -plane in a Gaussian fashion than that in the case these electrons initially have a uniform distribution on the  $xy$ -plane. More studies on this issue are worth performing in the future.

5. The non-thermal component of the energy spectrum has the shape of double power law, and the spectrum becomes hard in the range  $> 500$  keV. This is similar to

the energy spectra observed in the hard X-ray and  $\gamma$ -ray emissions of many flare, which showed hardening at around or above 300 keV (e.g., see Kong et al. 2013 and references therein). For the time being, its mechanism is not completely clear. One of the possible explanations is the shock formation in the reconnection region as proposed by Li et al. (2013b). Turbulent or cascading structures may also play a similar role. This is a topic worth of further experimental studies in the future.

6. The guide field also plays an apparent role in governing the formation of the fine structures in the reconnection region, and the direction of the reconnection outflows. The fine (turbulent) structures are easier to form in a guide Case (Figure 6b ) also indicated by the numerical experiments of Ni et al. (2015), and the guide field apparently changes the direction of the reconnection outflow in the environment of the plasma including heavy ions (see also Frank et al. 2006).

Finally, we need also note that the phenomenon we observed from the experiment is in 3D and our numerical experiments are indeed either in 2D or in 2.5D. The reason that we use 2D or 3D numerical experiments to explain the 3D phenomena is two-fold. First of all, in our experiments, magnetic reconnection occurs between the magnetic fields of opposite polarity entangling with expanding plasma bubbles created by the laser irradiation on the Al-foil. So if the two Al-foils are placed on the same plane, the reconnection process is confined to happen roughly on a plane in an approximately 2D fashion. Second, acceleration process in both experiments and numerical calculations lasts a very short time, and electrons move in the  $z$ -direction a very short distance (about 1 mm) before leaving the acceleration region. Therefore, the region of particle motion in the  $z$ -direction is actually finite in the simulation, and inside this region, the EM-field in the simulation can be considered roughly consistent with that in the experiment. Thus, to the lowest order of approximation, we use a 2D or 2.5D simulation to help us understand the fundamental

properties of the 3D phenomena for the time being. We should improve our numerical model in the future to better describe the experimental results and to better reveal physics of observations.

The authors are very much grateful to the SGII operation staff and the target preparation staff for valuable help and support. JL appreciates Nick Murphy for helpful discussions and suggestions. This work was supported by the 973 Program Grant 2013CBA01503, the NSFC Grants 11273033, 11205015, 11135012, 11220101002, 10821061, 11273055, and 11333007, CAS grant XDB09040202, and Beijing Nova Program Grant Z131109000413050.

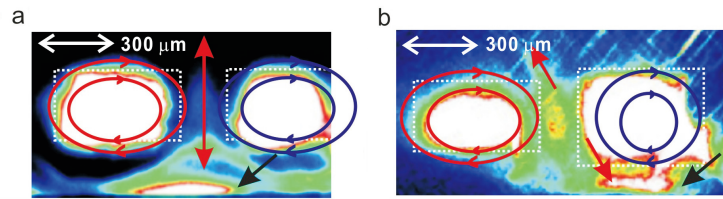


Fig. 6.— Patterns of the magnetic reconnection outflows in different cases. Magnetic field lines are illustrated based on the flux surface of the plasma bubbles in red and blue, respectively. In the case without the guide field (a), the outflows were ejected up- or down-ward normal to the surface of the Cu; and the direction of the outflow, together with the location of the “bench-top flare”, changes as the guide field exists (b).

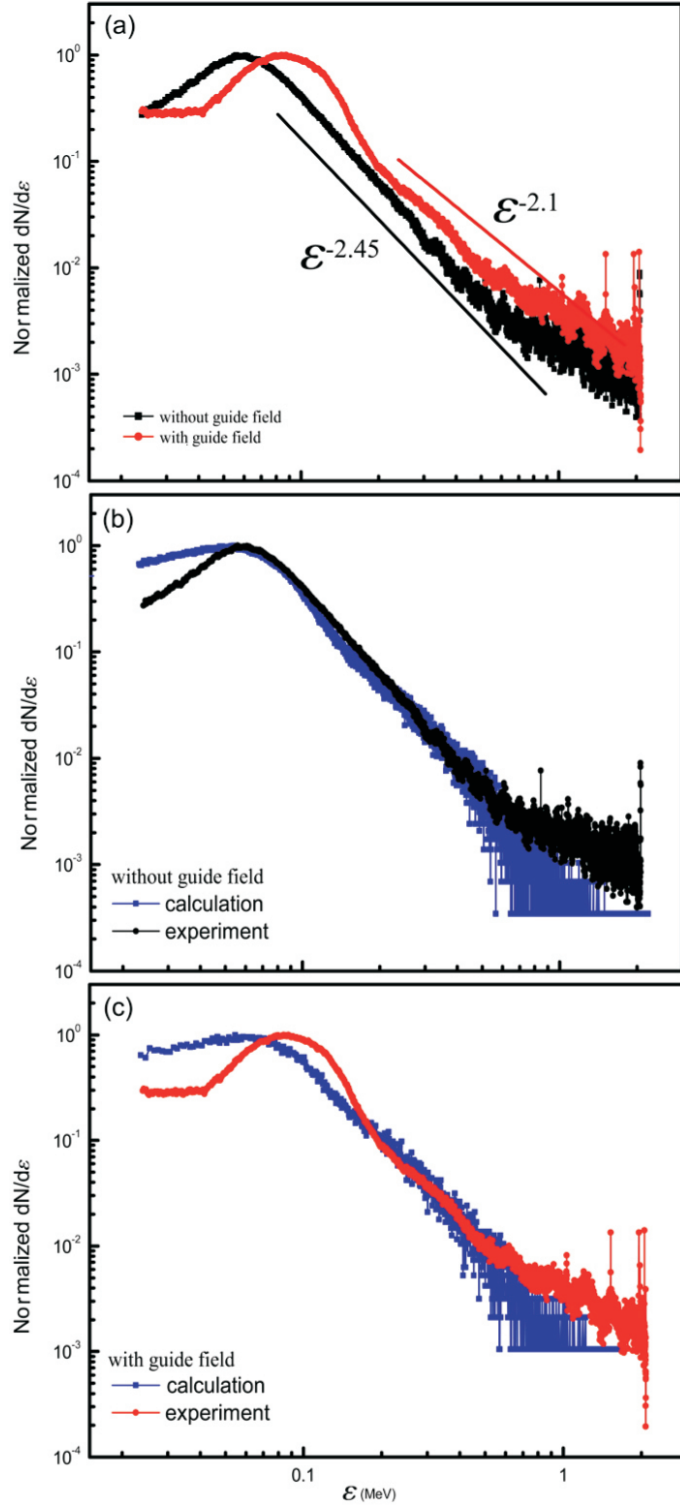


Fig. 7.— Differential energy spectra of energetic electrons. Two curves in panel (a) are from the experiments. Black and red curves in all three panels are for the cases without and with guide field in the EM-field, respectively. The blue curves in panels (b) and (c) result from numerical simulations which only considers the effect of the reconnecting electric field, and the thermal electrons distribute uniformly on the  $xy$ -plane prior to the acceleration (see text for more details).

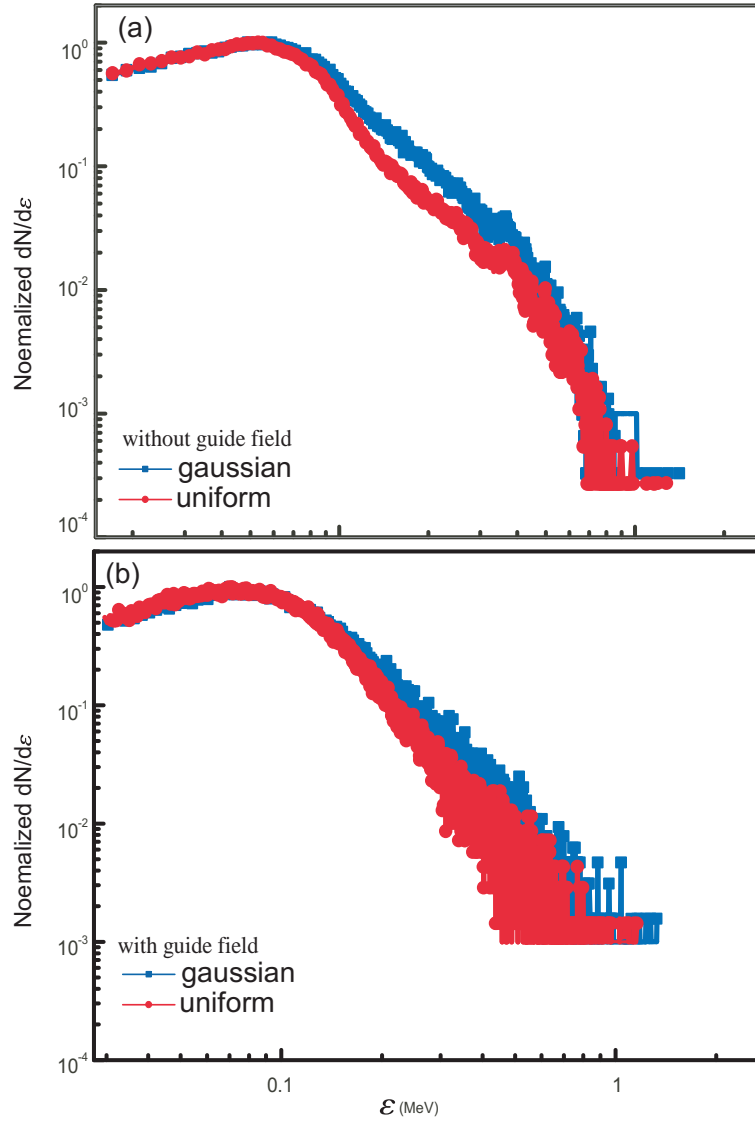


Fig. 8.— Differential energy spectra of energetic electrons accelerated in the EM-fields not including guide field (panel a) and including guide field (panel b) with uniform initial distribution (red) and Gaussian initial distribution (blue), respectively, for comparison.

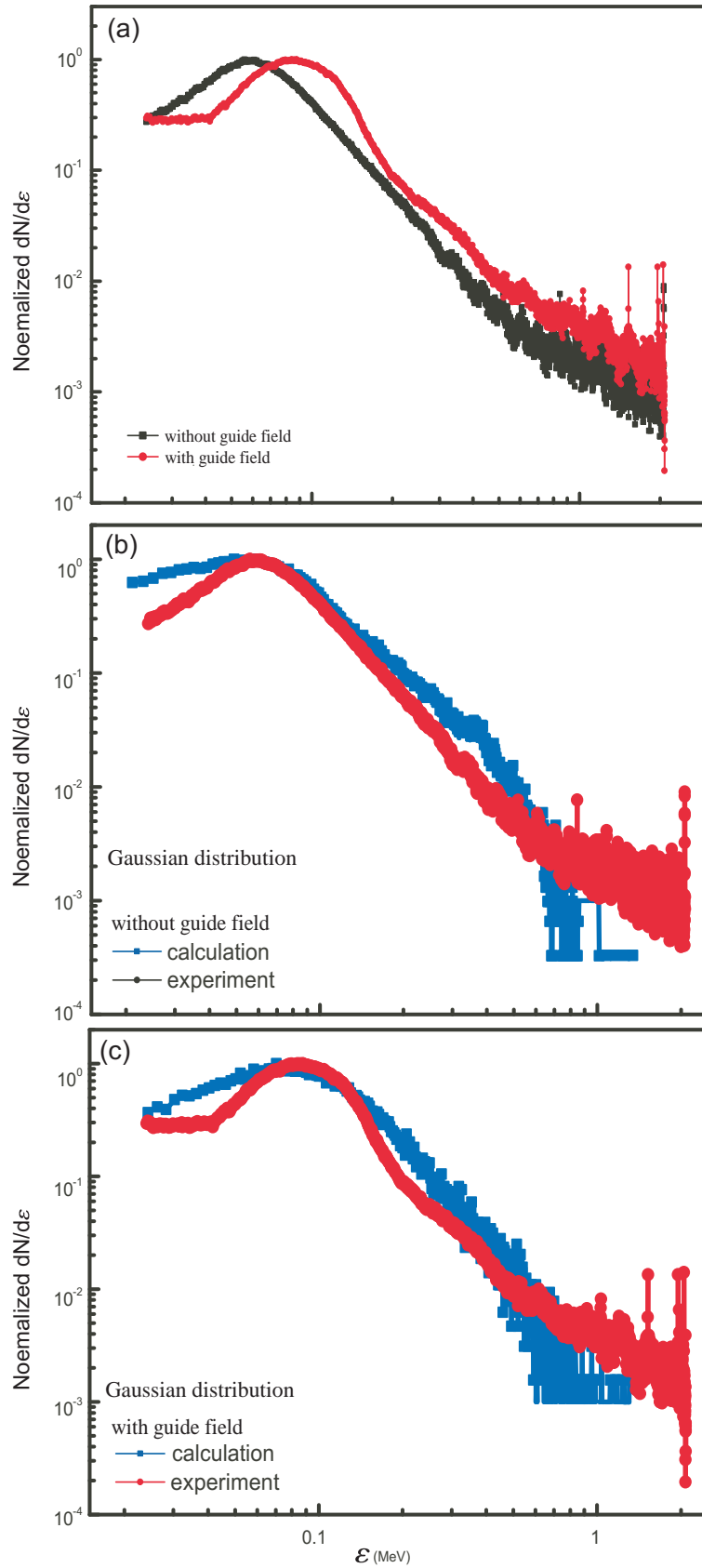


Fig. 9.— Same as Figure 7, but theoretical results in panels (b) and (c) correspond to that the thermal electrons distribute on the  $xy$ -plane in the Gaussian fashion before the acceleration begins.

## REFERENCES

- Adriani, O., Barbarino, G. C., Bazilevskaya, G. A., Bellotti, R., Beozio, M., Bogomolov, E. A., and another 46 co-authors. 2009, *Nature*, 458, 607
- Asai, A., Kiyohara, J., Takasaki, H., Narukage, N., Yokoyama, T., Masuda, S., Shimojo, M., & Nakajima, H. 2013, *Astrophys. J.*, 763, 87
- Aschwanden, M. J. 2002, *Space Sci. Rev.*, 101, 1-227
- Bárta, M., Buchner, J., Karlický, M., & Skala, J. 2011, *Astrophys. J.*, 737, 24
- Benka, S. G., & Holman, G. D. 1994, *Astrophys. J.*, 435, 469
- Bian, N. H., Emslie, A. G., Stackhouse, D. J., & Kontar, E. P. 2014, *Astrophys. J.*, 796, 142
- Biermann, L. 1950, *Zs. Naturforsch.*, 5a, 65
- Biskamp, D. 2000, *Magnetic Reconnection in Plasmas* (Cambridge University Press, New York)
- Bogdanov, S.Yu., Kyrie, N.P., Markov, V.S., & Frank, A.G. 2000, *JETP Lett.*, 71, 53
- Budden, K. G. 1961, *Radio Waves in the Ionosphere* (Cambridge University Press, Cambridge)
- Drake, J. F., Swisdak, M., Che, H., & Shay, M. A. 2006, *Nature*, 443, 553
- Dong, Q., et al. 2012, *Phys. Rev. Lett.* 108, 215001-215004 (2012).
- Emslie, A. G., Kontar, E. P., Krucker, S., & Lin, R. P. 2003, *Astrophys. J.*, 595, L107
- Emslie, A. G., Kucharek, H., & Dennis, B. R. 2004, *J. Geophys. Res.*, 109, A10104
- Forbes, T. G. & Acton, L. W. 1996, *Astrophys. J.*, 459, 330

- Fox, W., Bhattacharjee, A., & Germaschewski, K. 2011, *Phys. Rev. Lett.* 106, 215003
- Frank, A.G. 1999, *Plasma Phys. Controlled Fusion*, 41, A687
- Frank, A.G., & Bogdanov, S.Yu. 2001, *Earth Planets Space*, 53, 531
- Frank, A. G., Bogdanov, S. Yu., Dreiden, G. V., Markov, V. S., & Ostrovskaya, G. V. 2006, *Phys. Letters A*, 348, 318
- Helliwell, R. 2006, *Whistlers and Related Ionospheric Phenomena* (2nd ed.), Mineola, NY: Dover, pp. 23C24
- Hutchinson, I.M. 1987, *Principles of Plasma Diagnostics* (Cambridge University Press, Cambridge)
- Janvier, M., Aulanier, G., & Demoulin, P. 2015, *Solar Physics*, 290, 3425
- Jokipii, J. R. 1966, *Astrophys. J.*, 146, 480
- Jokipii, J. R. 1971, *Phys. Rev. Lett.*, 26, 666
- Kasparová, J., & Karlický, M. 2009, *Astron. & Astrophys.*, 497, L13
- Kong, X., Li, G., & Chen, Y. 2013, *Astrophys. J.*, 774, 140
- Ko, Y.-K., Raymond, J. C., Lin, J., Lawrence, G., Li, J., & Fludra, A. 2003, *Astrophys. J.*, 594, 1068
- Lazarian, A. & Vishniac, E. T. 1999, *Astrophys. J.*, 517, 700
- Lazarian, A., Vlahos, L., Kowal, G., Yan, H., Beresnyak, A., & Dal Pino, E. M. D. 2012, *Space Sci. Rev.*, 173, 557
- Lee, M. A., & Lerche, I. 1974, *Rev. Geophys. Sp. Phys.*, 12, 671.

- Li, C. K., et al. 2007, *Phys. Rev. Lett.*, 99, 055001
- Li, C. K. et al. 2009, *Phys. Rev. Lett.*, 102, 205001
- Li, G., Kong, X., Zank, G., & Chen, Y. 2013b, *Astrophys. J.*, 769, 22
- Li, Y., & Lin, J. 2012, *Sol. Phys.*, 279, 91
- Li, Y., Winter, H. D., Murphy, N. A., Lin, J., & Wu, N. 2013a, *Publ. Astron. Soc. Jpn.*, 65, 101
- Lin, J., Cranmer, S. R. & Farrugia, C. J. 2008, *J. Geophys. Res.* 113, A11107
- Lin, J., Ko, Y.-K., Sui, L., Raymond, J. C., Stenborg, G. A., Jiang, Y., Zhao, S., Mancuso, S. 2005, *Astrophys. J.*, 622, 1251
- Lin, J. Murphy, N. A., Shen, C., Raymond, J. C., Reeves, K. K., Zhong, J., Wu, N., & Li, Y. 2015, *Space Sci. Rev.*, 194, 237
- Lin, R. P., & Hudson, H. S. 1976, *Sol. Phys.*, 50, 153
- Litvinenko, Y. E. 1996, *Astrophys. J.*, 462, 997
- Loeb, A., & Eliezer, S. 1986, *Phys. Rev. Lett.*, 56, 2252
- Mandrini, C. H., Baker, D., & Demoulin, P., et al. 2015, *Astrophys. J.*, 809, 73
- Martens, P. C. H. 1988, *Astrophys. J.*, 330, L131
- Martens, P. C. H., & Young, A. 1990, *Astrophys. J. Suppl. S.*, 73, 333
- Mei, Z., Shen, C., Wu, N., Lin, J., Murphy, N. A., Roussev, I. I. 2012, *Mon. Not. R. Astron. Soc.*, 425, 2824

- Meng, Y., Lin, J., Zhang, L., Reeves, K. K., Zhang, Q. S., & Yuan, F. 2014, *Astrophys. J.*, 785, 62
- Miller, J. A., Cargill, P. J., Emslie, A. G., et al. 1997, *J. Geophys. Res.*, 102, 14631
- Miller, J. A. 1998, *Space Sci. Rev.*, 86, 79
- Murphy, N. A., & Sovinec, C. R. 2008, *Phys. Plasmas*, 15, 042313
- Ni, L., Lin, J., Mei, Z., & Li, Y. 2015, *Astrophys. J.*, 812, 92
- Nilson, P. M., et al. 2006, *Phys. Rev. Lett.*, 97, 255001
- Nilson, P. M., et al. 2008, *Phys. Plasmas*, 15, 092701
- Perez, F., Kemp, A. J., Divol, L., Chen, C. D., & Patel, P. K. 2013, *Phys. Rev. Lett.*, 111, 245001
- Petschek, H. E., 1964, in Hess W. N., ed., *Proc. AAS-NASA Symp. Vol. 50, The Physics of Solar Flares*. NASA, Science and Technical Information Division, Washington, DC, p. 425
- Priest, E. R. 2014, *MHD of the Sun*. Cambridge, UK: Cambridge University Press
- Priest, E. R., & Forbes, T. G. 2000, *Magnetic Reconnection: MHD Theory and Applications*, (New York:Cambridge Univ. Press)
- Pritchett, P. L. 2001, *J. Geophys. Res.*, 106, 25961
- Pritchett, P. L., & Coroniti, F. V. 2004, *J. Geophys. Res.*, 109, A01220
- Reames, D. V. 1998, *Space Sci. Rev.*, 85, 327
- Reames, D. V. 2013, *Space Sci. Rev.*, 175, 53

- Remington, B. A., Drake, R. P., & Ryutov, D. D. 2006, *Rev. Mod. Phys.*, 78, 755
- Roxburgh, I. W. 1966, *Mon. Not. R. Astron. Soc.*, 132, 201
- Ryutov, D. D., Drake, R. P., & Remington, B. A. 2000, *Astrophys. J. Suppl. S.*, 127, 465
- Share, G. H., & Murphy, R. J. 2006, *Geoph Monog Series*, 165, 177
- Shen, C. C., Lin, J., & Murphy, N. A. 2011, *Astrophys. J.*, 737, 14
- Silva, A. V. R., Wang, H., & Gary, D. E. 2000, *Astrophys. J.*, 545, 1116
- Speiser, T. W. 1965, *J. Geophys. Res.*, 70, 4219
- Stamper, J. A., & Ripin, B. H. 1975, *Phys. Rev. Lett.*, 34, 138
- Suri, A. N., Chupp, E. L., Forrest, D. J., & Reppin, C. 1975, *Sol. Phys.*, 43, 415
- Svestka, Z. 1976, *Solar flares*. Springer-Verlag Berlin Heidelberg, pp. 415.
- Tharp, T. D., Yamada, M., Ji, H., Lawrence, E., Dorfman, S., Myers, C. E., & Yoo, J. 2012, *Phys. Rev. Lett.*, 109, 165002
- Thorne, R. M., O'Brien, T. P., Shprits, Y. Y., Summers, D., & Horne, R. B. 2005, *J. Geophys. Res.*, 110, A09202
- Tsuneta, S, & Naito, T. 1998, *Astrophys. J.*, 495, L67
- Wentzel, D. G. 1974, *Annu. Rev. Astron. Astrophys.*, 12, 71.
- Widrow, L. M. 2002, *Rev. Mod. Phys.*, 74, 775
- Xu, Y., Emslie, A. G., & Hurford, G. J. 2008, *Astrophys. J.*, 673, 576
- Yamada, M. 2007, *Phys. Plasmas*, 14, 058102

Yates, M. A., et al. 1982, *Phys. Rev. Lett.*, 49, 1702

Yoshimori, M., Watanabe, H., & Nitta, N. 1985, *JPSJ*, 54, 4462

Yuan, F., & Zhang, B. 2012, *Astrophys. J.*, 757, 56-60

Zhao, L., & Li, G. 2014, *J. Geophys. Res.*, 119, A020103

Zharkova, V. V., et al. 2011, *Space Sci. Rev.*, 159, 357

Zhong, J. Y., et al. 2010, *Nat. Phys.*, 6, 984